# Using the Sensitivity of Large-Eddy Simulations to Evaluate Atmospheric Boundary Layer Models

GILLES BELLON

*Centre National de Recherches Météorologiques, CNRS/Météo-France, Toulouse, France*

BJORN STEVENS

*Max Planck Institut für Meteorologie, Hamburg, Germany*

(Manuscript received 15 June 2011, in final form 27 September 2011)

## ABSTRACT

A simple framework to study the sensitivity of atmospheric boundary layer (ABL) models to the large-scale conditions and forcings is introduced. This framework minimizes the number of parameters necessary to describe the large-scale conditions, subsidence, and radiation. Using this framework, the sensitivity of the stationary ABL to the large-scale boundary conditions [underlying sea surface temperature (SST) and overlying humidity and temperature in the free troposphere] is investigated in large-eddy simulations (LESs). For increasing SST or decreasing free-tropospheric temperature, the LES exhibits a transition from a cloud-free, well-mixed ABL stationary state, through a cloudy, well-mixed stationary state and a stable shallow cumulus stationary state, to an unstable regime with a deepening shallow cumulus layer. For a warm SST, when increasing free-tropospheric humidity, the LES exhibits a transition from a stable shallow cumulus stationary state, through a stable cumulus-under-stratus stationary state, to an unstable regime with a deepening, cumulus-under-stratus layer. For a cool SST, when increasing the free-tropospheric humidity, the LES stationary state exhibits a transition from a cloud-free, well-mixed ABL regime, through a well-mixed cumulus-capped regime, to a stratus-capped regime with a decoupling between the subcloud and cloud layers.

This dataset can be used to evaluate other ABL models. As an example, the sensitivity of a bulk model based on the mixing-line model is presented. This bulk model reproduces the LES sensitivity to SST and free-tropospheric temperature for the stable and unstable shallow cumulus regimes, but it is less successful at reproducing the LES sensitivity to free-tropospheric humidity for both shallow cumulus and well-mixed regimes.

## 1. Introduction

Tropical marine boundary layer clouds are a large source of uncertainties in estimates of climate change using climate models (Bony and Dufresne 2005; Dufresne and Bony 2008). Our understanding of the influence of large-scale conditions on the local cloud cover is limited despite extensive observational work at various time scales: statistically, the low-cloud cover is linked to the sea surface temperature (SST), lower-tropospheric stability (LTS), sea level pressure, and subsidence (Klein and Hartmann 1993; Norris and Leovy 1994; Norris and Klein 2000; Clement et al. 2009), but the mechanisms behind these controls are still poorly understood. This limits our ability to improve the parameterization of the atmospheric boundary layer (ABL) processes in climate models.

With the constant growth of computing resources, large-eddy simulations (LESs) have become a popular tool to try to understand different aspects of the ABL processes, from the lateral entrainment and detrainment in shallow cumulus (Siebesma and Cuijpers 1995) to the influence of aerosols on precipitation (Xue et al. 2008). These simulations have been evaluated through comparisons to field measurements (Moeng et al. 1996; Stevens et al. 2001; Siebesma et al. 2003; Stevens et al. 2005; Brown et al. 2006; Stevens et al. 2007; Ackerman et al. 2009) within the Global Energy and Water Experiment (GEWEX) Cloud System Study (GCSS) Boundary

*Corresponding author address:* Gilles Bellon, Centre National de Recherches Météorologiques, 42, avenue Gaspard Coriolis, 31057 Toulouse, France.
E-mail: gilles.bellon@meteo.fr

Layer Cloud Working Group (BLCWG). The success of the LES in reproducing important features of the observations has encouraged their use in the evaluation of single-column models and general circulation model (GCM) parameterizations (Bechtold et al. 1996; Lenderink et al. 2004; Zhu et al. 2005; Wyant et al. 2007).

In the present study, we propose an idealized framework to study the sensitivity of ABL models to the large-scale conditions (boundary conditions and forcings) using as few parameters as possible. We use the University of California, Los Angeles (UCLA) LES code in this framework to study the sensitivity of the ABL stationary state to the large-scale thermodynamic conditions (SST, free-tropospheric temperature, and humidity). This work aims both at achieving a better theoretical understanding of the key large-scale controls on low-cloud fraction and at proposing a validation approach for other models and parameterizations, complementary to the case studies of the GCSS BLCWG or the single-site strategy proposed by Neggers et al. (2012); indeed, the LES sensitivity experiments can be used as a benchmark to validate the sensitivity of other models. Rather than investigating the time-dependent response to one set of forcings as in a case study, we focus on the stationary response to a change in forcings.

The next section introduces the LES code and the framework, section 3 presents the results of our LES sensitivity experiments, and section 4 illustrates the proposed validation approach with bulks models before our conclusions in section 5.

## 2. LES and idealized large-scale conditions

### a. Model summary

We use the UCLA LES in a nonprecipitating configuration. The basic code is the same as described in Stevens et al. (2005); it solves the Ogura–Phillips anelastic equations using finite differences on a regular horizontal, stretched vertical mesh. The prognostic variables are the three components of the velocity ($u$, $v$, $w$) and two variables specifying the thermodynamic state: the total water mixing ratio $q_t$ and the liquid water potential temperature $\theta_l$. Cloud and microphysical processes are represented following the procedures described by Savic-Jovcic and Stevens (2008).

We run the model over a square horizontal domain of 6.4 km × 6.4 km, with a horizontal resolution of 50 m in both direction. We use 121 vertical levels with a 10-m resolution at the surface increasing by 2% at each level so that the domain tops at 4830 m. These resolutions are coarse by current standards but, considering current computing resources, this coarseness is a necessary trade-off

against the need to run many simulations (for an extended range of forcings) for long periods of time (in order to explore the equilibrium structure of the equations). Spatial resolution and subgrid schemes, as well as domain size, have been shown to influence LES results (Matheou et al. 2011), especially in term of liquid water and cloud fraction. In the absence of interactive radiation and microphysical processes, the LES sensitivity to resolution is diminished and, although not negligible, we expect the differences between single-column models and LES to be significantly larger than this numerical sensitivity. To address this issue, we conducted a few sensitivity experiments with increased horizontal and vertical resolution for well-mixed ABLs. We found that the main characteristics of the ABL as simulated at lower resolution are conserved, and that the equilibrium response of the LES as a function of large-scale parameters is not qualitatively sensitive to modest changes in resolution, although the thresholds between regimes shift slightly. The details of these sensitivity tests are discussed in appendix A.

### b. Idealized large-scale conditions

Our aim is to develop a simple framework that describes the large-scale forcings and boundary conditions of the LES with a small number of parameters. We also want these large-scale fields and forcings to be balanced in the absence of turbulence above the inversion.

In LESs, horizontal wind divergence is often prescribed to be constant; this corresponds to a subsidence that increases monotonically with altitude. In the real subsiding atmosphere, large-scale subsidence increases with altitude in the lower troposphere and tends to be almost constant in the middle troposphere before decreasing in the upper troposphere. To mimic the lower half of this type of profile with a minimum of parameters, we choose to prescribe a subsidence profile that uses an exponential of altitude:

$$w(z) = -w_0(1 - e^{-z/z_w}), \tag{1}$$

where $w(z)$ is the large-scale vertical velocity at altitude $z$, which is described by two parameters: $w_0$, the high-altitude asymptotic value of subsidence ($w_0 > 0$ for subsidence), and $z_w$, a typical vertical scale of large-scale dynamics. The divergence at the surface is $D_0 = w_0/z_w$ and it decreases exponentially with altitude.

We choose to neglect the large-scale horizontal advection of humidity and to consider that radiation and the large-scale horizontal advection of energy can be modeled like a prescribed, altitude-independent cooling $R$ ($R > 0$ for cooling) that applies to potential temperature. The exclusion of cloud radiative forcing

TABLE 1. Boundary conditions used in the sensitivity experiments.

| Boundary conditions | Sensitivity to | | | |
| --- | --- | --- | --- | --- |
| | SST | Free-tropospheric temperature | Free-tropospheric humidity (ShCu) | Free-tropospheric humidity (well mixed) |
| $T_s$ (K) | 294–302 | 300 | 300 | 296 |
| $\theta_r$ (K) | 315 | 313–320 | 315 | 315 |
| $q_0$ (g kg$^{-1}$) | 4 | 4 | 2–10 | 2–14 |

can impact the stratocumulus regime but it should not be a strong constraint for regimes with small liquid water path or small cloud fractions such as the shallow cumulus regime.

Once the large-scale forcing is prescribed, the water and energy balance of the nonturbulent troposphere imposes the free-tropospheric profiles of humidity $q_{ft}$ and potential temperature $\theta_{ft}$:

$$q_{ft}(z) = q_0, \qquad (2)$$

$$\partial_z \theta_{ft} = \frac{R}{w_0(1 - e^{-z/z_w})},$$

$$\theta_{ft}(z) = \frac{R}{w_0} z_w \ln(e^{z/z_w} - 1) + \theta_0, \qquad (3)$$

where $q_0$ and $\theta_0$ prescribe the uniform free-tropospheric specific humidity and the reference temperature at $z = z_w$ in Eq. (2).

We also set a constant SST $T_s$ and a constant geostrophic zonal wind $U$ (the latitude is set to 20°N). Our large-scale conditions and forcing are thus controlled by seven parameters: $w_0, z_w, R, U, T_s, q_0$, and $\theta_0$. In practice, this last parameter is replaced by the potential temperature $\theta_r$ at 4000 m. In the present study, we examine the sensitivity of the LES stationary state to the thermodynamic large-scale conditions: we vary systematically $T_s$, $q_0$, and the 4000-m potential temperature $\theta_r$. This framework has been used by Nuijens and Stevens (2012) to study the sensitivity of the boundary layer to perturbations in wind speed.

### c. Control cases and sensitivity studies

We design a shallow cumulus (ShCu) control case that roughly resembles the Barbados Oceanographic and Meteorological Experiment (BOMEX) case (Siebesma et al. 2003; Holland and Rasmusson 1973). The radiative cooling is set to 2 K day$^{-1}$. The geostrophic wind is set to $U = 10$ m s$^{-1}$. The free-tropospheric subsidence is set to $w_0 = 7.5$ mm s$^{-1}$ and the vertical scale of subsidence is set to $z_w = 1200$ m; this corresponds to a surface divergence of $D_0 = 6.25 \times 10^{-6}$ s$^{-1}$. The free-tropospheric humidity is set to $q_0 = 4$ g kg$^{-1}$ and the 4000-m potential temperature is set to $\theta_r = 315$ K. In the shallow convective

control case, the SST is set to 300 K. We also design a well-mixed control case with the same large-scale forcing and free-tropospheric conditions, but with a lower SST of 296 K. In all cases, the surface pressure is set to 1015.4 hPa.

We allow the simulations to continue until they reach stationarity (if they do). This requires 1–2 weeks of model integration in the cases we present here. We define stationarity based on the the 6-h-mean altitude $h$ of the top of the inversion, which should be steady for 24 h. In the LES, the altitude of the top of the inversion, which we consider equivalent to the ABL depth, is defined as the lowest altitude where $q_t(h) - q_0 \leq 0.01$ g kg$^{-1}$. Cases that do not seem to approach stationarity after 12 days are stopped and defined as unstable.

We study the sensitivity of the LES stationary state (as described by the 6-h mean state when stationarity is reached) to the SST boundary conditions. We also investigate the sensitivity of the shallow convective case to the free-tropospheric humidity and temperature, and the sensitivity of the well-mixed case to the free-tropospheric humidity. Table 1 shows the range of boundary conditions used in these experiments.

For the ShCu control run, we use the same initial profiles of $\theta_l$ ans $q_t$ as in the BOMEX LES intercomparison (Siebesma et al. 2003) up to the altitudes where they reach the free-tropospheric reference profiles (2000 m for $\theta_l$ and 2170 m for $q_t$), and $\theta_l$ and $q_t$ are set to the reference profiles above these altitudes. The initial wind profile is set to the geostrophic wind. For the sensitivity experiments, we construct initial profiles using the stationary profiles of the previous stable case with the most similar large-scale conditions: when varying the SST, we use the stationary profiles with closest SST as initial conditions; when varying $q_0$, we use the stationary profiles of $u$, $v$, and $\theta_l$ with closest $q_0$ as initial conditions, and we use the corresponding profile of $q_t$ to construct an initial humidity profile that matches the new free-tropospheric humidity. More specifically, when increasing $q_0$, the initial $q_t$ profile is the closest stationary profile up to the level where $q_t$ reaches the new $q_0$, and $q_0$ above. When decreasing $q_0$, the initial $q_t$ profile is the closest stationary profile up to the level of maximum vertical gradient of $q_t$ where it becomes linear up to the new $q_0$. The same method is applied to construct initial profiles when varying $\theta_r$.
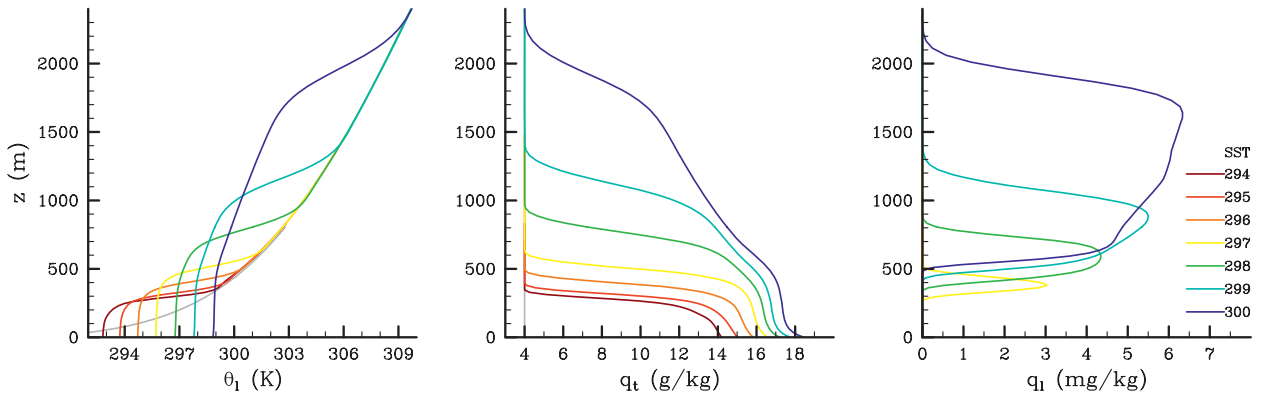
FIG. 1. Stationary mean profiles of (left) liquid water potential temperature, (middle) total water mixing ratio, and (right) liquid water mixing ratio for different values of SST. Reference free-tropospheric profiles are shown by gray lines.

## 3. LES results

In our shallow cumulus control case, the LES reaches a stationary cloudy boundary layer similar to that observed in the BOMEX case. Figure 1 shows the stationary mean vertical profiles of liquid water potential temperature, total water mixing ratio, and liquid water mixing ratio (blue lines). In the ShCu control case, a cloud layer extends from an altitude of 500 m to the top of the inversion at 2250 m, over a well-mixed subcloud layer. The main difference with the BOMEX case is that the maximum of liquid water is located in the upper part of the cloud layer rather than near the cloud base.

In our well-mixed control case (orange lines in Fig. 1), the LES reaches a stationary state with a fairly well-mixed, essentially cloud-free ABL that tops at 500 m (in the present work, the ABL is defined as extending from the surface to the top of the inversion).

### a. ABL sensitivity to SST

We run LESs for varying SST from 294 to 302 K, with a 1-K step. For $T_s \leq 300$ K, the LES reaches a stationary state. Figure 1 shows the simulated stationary mean profiles of the thermodynamic variables. For $T_s \leq 298$ K, the LES yields a shallow, well-mixed ABL that is cloud-free for $T_s \leq 296$ K and is topped by cumulus humilis for $T_s = 297$ K. The case with $T_s = 296$ K is right at the transition between cloud-free and cloudy ABL: an occasional cumulus humilis is produced. For $298 \leq T_s \leq 300$ K, the LES yields a shallow convective ABL with clouds tending toward cumulus mediocris with increasing SST.

For higher SST ($T_s \geq 301$ K), the LES produces an ever-growing ABL. As an example, Fig. 2 shows 3 days of the simulation with $T_s = 301$ K. Figure 2 shows that the subcloud layer is almost stationary, while the cloud layer deepens at a fairly constant rate. This linear growth
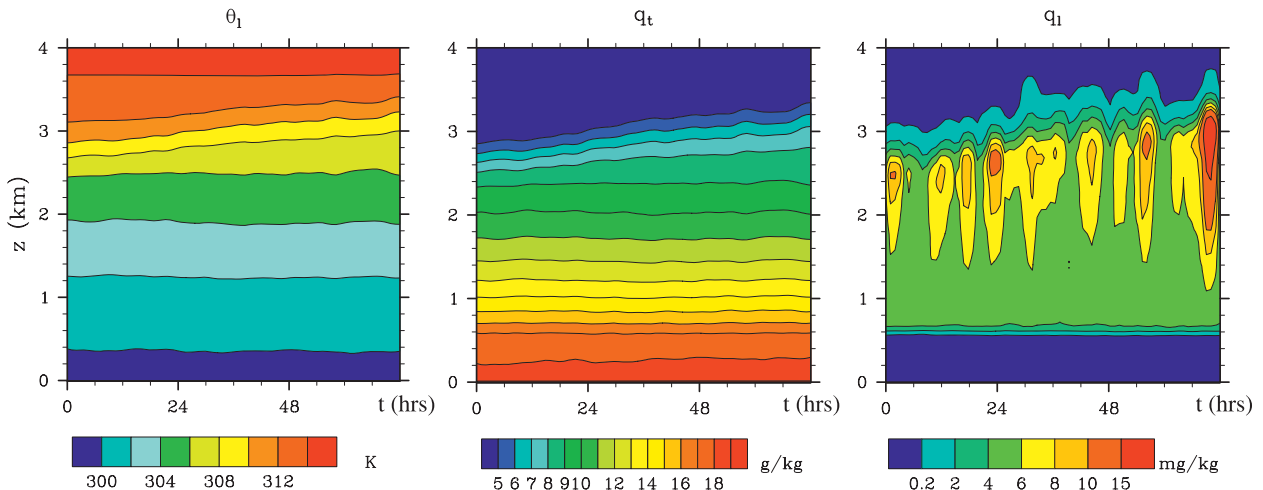


FIG. 2. Time evolution of 3-h-running-average (left) liquid water potential temperature, (middle) total water mixing ratio, and (right) liquid water mixing ratio for SST = 301 K (days 10–12 of the simulation).

of the layer has been described by Stevens (2007), suggesting that the mechanism responsible for this growth is the injection/evaporation mechanism: liquid water is injected in the inversion layer by convective plumes and evaporates, cooling and moistening the inversion layer until its properties are similar to those at the top of the cloud layer (Stevens 2007). The stationarity of the subcloud layer results from a fast adjustment of temperature and humidity at the beginning of the simulation (not shown). This fast adjustment of the subcloud layer and the slower evolution of the cloud layer and ABL height are similar to previous results on ShCu ABLs (Bretherton and Park 2008), and the time scale separation is similar to that obtained in simulations of well-mixed ABLs (Bretherton et al. 2010; Schubert et al. 1979). After the fast adjustment of the subcloud temperature and humidity, the surface fluxes are almost stationary as well.

The simulated depth of the well-mixed layer $\eta$ and inversion top $h$, ABL growth rate, conserved variables in the well-mixed layer, and surface turbulent fluxes are presented as a function of SST in Fig. 3. Filled circles indicate stationary states, and open circles indicate the almost stationary variables (subcloud variables, surface fluxes, and ABL growth rate) in the unstable cases. As defined in section 2c, the inversion top $h$ is the altitude where the total water mixing ratio reaches the free-tropospheric value. For LES of cloudy ABLs, the well-mixed layer is the subcloud layer whose top $\eta$ is defined by the cloud base (i.e., the lowest level where the liquid water is positive). For LES of cloud-free ABLs, we define $\eta$ as the altitude where the buoyancy flux departs significantly (i.e., by 10%) from a linear profile: the well-mixed layer top is defined as the first level where the gradient of buoyancy flux becomes larger (i.e., smaller in absolute value) than 90% of the vertically averaged gradient between the surface and this level:

$$\partial_z \overline{w'b'}(\eta) \approx 0.9 \frac{\overline{w'b'}(\eta) - \overline{w'b'}(0)}{\eta}. \tag{4}$$

This definition was found to be a fair match to the cloud base in the cloudy cases.

The well-mixed conserved variables $\theta_M$ and $q_M$ are the vertical averages of $\theta_l$ and $q_t$ between the surface and $\eta$:

$$\phi_M = \int_0^\eta \phi(z) \frac{dz}{\eta},$$

where $\phi$ is the liquid potential temperature $\theta_l$ or the total water mixing ratio $q_t$.

For stable cases, the ABL deepens nonlinearly with SST (Fig. 3a), and the ABL growth increases sharply with

SST for $T_s > 300$ K (Fig. 3b). The subcloud (or well-mixed) potential temperature $\theta_M$ closely follows the SST (Fig. 3c), and the subcloud specific humidity $q_M$ increases linearly with increasing SST as well (Fig. 3d). The sensitivity of the surface sensible heat flux (SHF) is small and nonmonotonic (Fig. 3e). On the other hand, because of the nonlinearity of Clausius–Clapeyron, the surface latent heat flux (LHF) increases with SST (Fig. 3f). From an energetics point of view, it is the LHF that causes the deepening of the stationary-state ABL with increasing SST and fuels the ABL instability at high SST.

Figure 4 shows the sensitivity of stationary mean cloud fraction and liquid water path (LWP) to SST. The cloud fraction increases almost linearly for $T_s \gtrsim 297$ K, and remains small, below 15%. LWP increases in a nonlinear fashion, mostly because of the nonlinear growth of the cloud-layer depth. In the unstable cases, the cloud fraction and LWP grow indefinitely, but the cloud fraction remains moderate, below 18% after 12 days of simulation (see Fig. 4) even for clouds that extend almost to the top of the domain (4.8 km), as is the case at the end of the 12-day simulation for SST = 302 K. None of our simulations with varying SST yields a large cloud cover.

The sensitivity of the simulated ABL vertical structure conforms to our expectations: ABL depth is expected to increase with increasing SST (i.e., decreasing LTS) because the buoyancy of surface parcels increases with SST (compared to free-tropospheric buoyancy); our LES yield a ShCu stable regime for a limited range of LTS (from about 11 to 15 K). The sensitivity of the cloud cover is more of a surprise: we would expect the cloud fraction to have a maximum in a stratus well-mixed regime between the cloud-free, well-mixed regime and the ShCu regime to match the observed climatological correlation between cloudiness and LTS (Klein and Hartmann 1993; Clement et al. 2009) or other measures of the stability accross the ABL (Wood and Bretherton 2006). Our LESs do not exhibit such a stratus regime; this may result from the absence of cloud–radiative feedbacks.

### b. ABL sensitivity to free-tropospheric temperature

We repeat the simulations for varying 4000-m potential temperature, from 313 to 320 K, with a 1-K step. For $\theta_r \gtrsim 315$ K, the LES reaches stationarity. Figure 5 shows the simulated stationary mean profiles of the thermodynamic variables. For $\theta_r = 320$ K, the LES yields a cloud-free, well-mixed ABL. For $\theta_r = 318$ and 319 K, the LES yields a well-mixed ABL capped by small, shallow cumuli that deepen with decreasing $\theta_r$. For $315 \leq \theta_r \leq 317$ K, the LES reaches a ShCu stationary state that deepens with decreasing $\theta_r$.

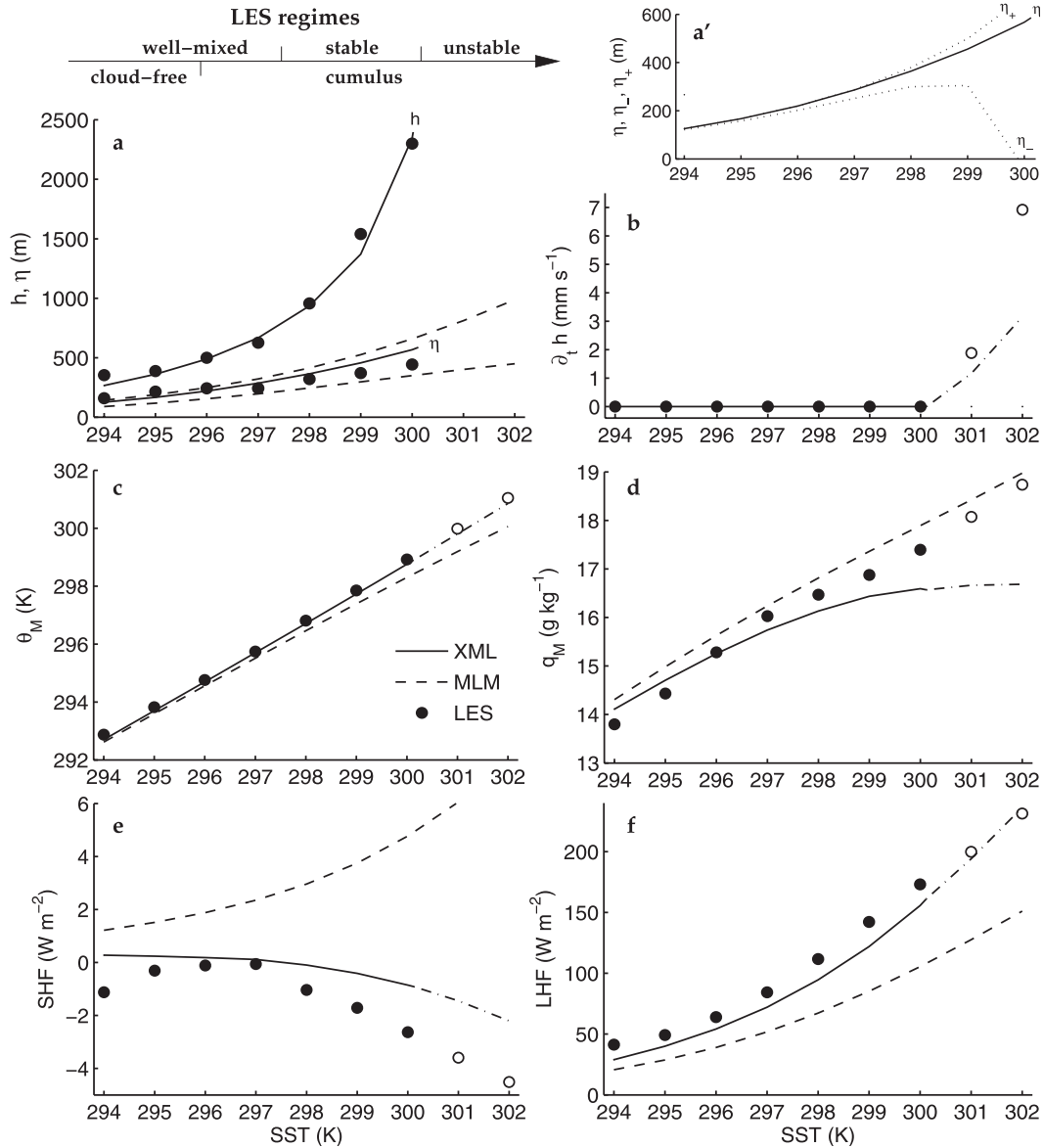For lower tropospheric temperature ($\theta_r = 314$ and 313 K), the LES produces an ever-growing ShCu ABL

FIG. 3. Sensitivity to SST of (a) ABL depth $h$ and depth of the well-mixed layer $\eta$, (b) ABL growth, (c) well-mixed potential temperature, (d) well-mixed specific humidity, (e) surface sensible heat flux, and (f) surface latent heat flux. LES stationary states are shown by filled circles, and almost-stationary variables from unstable LES cases are shown by open circles. XLM steady states are shown by solid lines and steady variables from unstable XLM cases are shown by dash-dotted lines. MLM model steady states are shown by dashed lines; in (a), the dashed lines show the MLM ABL depth $h$ and cloud base (LCL). (a') The XLM $\eta$ [reproduced from (a)] and its bounds $\eta^-$ and $\eta^+$.

very similar to the cases with high SSTs: the surface fluxes, the subcloud temperature, and humidity are almost stationary, as well as the ABL growth rate. In summary, the sensitivity of the LES to increasing free-tropospheric temperature is very similar to its sensitivity to decreasing SST. Subcloud temperature and humidity, ABL depth and growth, surface fluxes, cloud fraction, and LWP exhibit similar sensitivities as shown in Figs. 3 and 4 (except for an opposite direction of the $x$ axis; not shown). The

main difference is the sensitivity of $q_M$ that increases with $\theta_r$ (i.e., decreases with $h$), as can be seen from the middle panel in Fig. 5. The ABL humidity results from a balance between evaporation and ventilation by the subsidence at the inversion; as the ABL shoals, the subsidence at the top of the inversion decreases and causes a decrease in ventilation that results in a moistening of the ABL. This process dominates as $\theta_r$ is increased, whereas the change in surface evaporation plays a decisive role when the SST
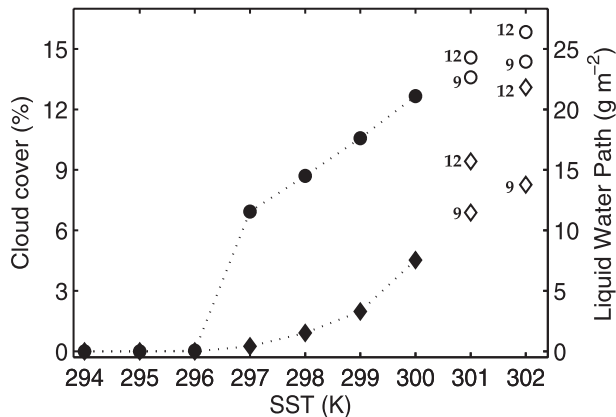
FIG. 4. Sensitivity of the stationary mean cloud fraction (circles) and liquid water path (diamonds) to SST. Stationary means are shown by filled markers and selected daily averages are shown by open markers for the unstable cases (days 9 and 12 of integration are indicated by "9" and "12" labels).

decreases for the same change in LTS. This sensitivity of $q_M$ is in turn responsible for a decrease of evaporation with decreasing $h$ (i.e., increasing $\theta_r$) that is similar to the covariation of $h$ and LHF with varying SST.

As in the case of a varying SST, our LES yields a stable ShCu regime for an LTS in the 11–15-K range when $\theta_r$ is varied. This suggests that the main influence of SST and free-tropospheric temperature on the ABL depth acts through the LTS (or some similar measure of the stability in the lower troposphere).

### c. Sensitivity of a shallow convective ABL to free-tropospheric humidity

We repeat the simulations for an SST of 300 K and a varying free-tropospheric specific humidity, from 2 to 10 g kg$^{-1}$, with a 2 g kg$^{-1}$ step. For $q_0 \leq 8$ g kg$^{-1}$, the LES reaches a ShCu stationary state. Figure 6 shows the simulated stationary mean profiles of the thermodynamic

variables. The simulated ABL deepens with increasing $q_0$; it also moistens, but most significantly at the top of the cloud layer, where a stratiform cloud develops for $q_0 > 6$ g kg$^{-1}$: the LES yields a cumulus-under-stratus regime for large free-tropospheric humidity. The vertical gradient of liquid potential temperature in the cloud layer decreases with increasing $q_0$; this suggests that, at the top of the cloud layer, the moister (i.e., closer to saturation) the air entrained from above, the less efficient the evaporative cooling.

For $q_0 = 10$ g kg$^{-1}$, the LES yields simulates an ever-growing ABL. Figure 7 shows days 2–4 of the simulation (using the $q_0 = 8$ g kg$^{-1}$ stationary mean profiles as initial conditions). The cloud plumes start interacting with the saturated upper part of the domain during the fifth day of integration. As in the unstable cases with high SSTs, the subcloud layer is almost stationary, while the cloud layer deepens at a fairly constant rate. The liquid water in the stratiform cloud above the small cumulus increases up to an order of magnitude larger than the typical ShCu liquid water.

We also ran simulations for higher free-tropospheric specific humidity, but because our framework specifies a uniform free-tropospheric humidity, a significant fraction of the domain is saturated (above 3000 m), and in these simulations cloud plumes start interacting with this saturated upper-domain shortly after the beginning of the simulation. These simulations are thus unsuitable for our analysis of the ABL dynamics; from the beginning of the simulations, it appears that cases for $q_0 = 12$ and 14 g kg$^{-1}$ are similar to the case with $q_0 = 10$ g kg$^{-1}$ with a faster ABL growth.

Figure 8 shows the sensitivity of the stationary cloud fraction and liquid water path to $q_0$. Both the cloud fraction and LWP increase moderately with free-tropospheric humidity up to $q_0 = 8$ g kg$^{-1}$. In the unstable cases ($q_0 = 10$ g kg$^{-1}$), the cloud fraction and LWP grow constantly
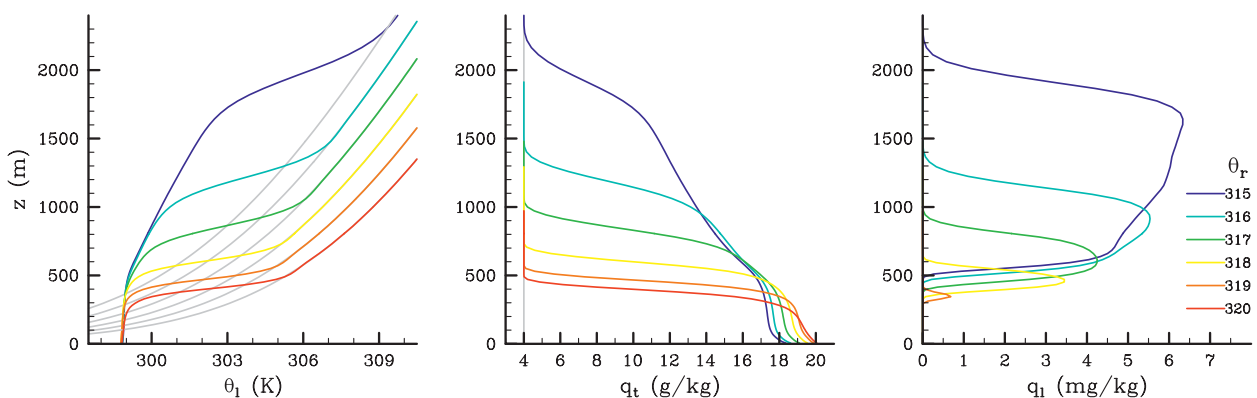


FIG. 5. Stationary mean profiles of (left) liquid water potential temperature, (middle) total water mixing ratio, and (right) liquid water mixing ratio for different values of the potential temperature $\theta_r$ at 4 km. Reference free-tropospheric profiles are shown by gray lines.
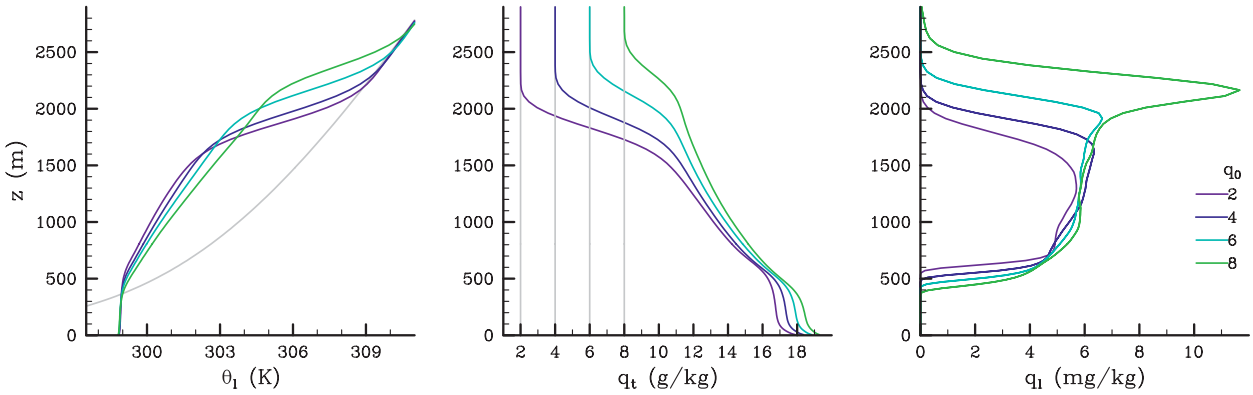
FIG. 6. Stationary mean profiles of (left) liquid water potential temperature, (middle) total water mixing ratio, and (right) liquid water mixing ratio for different values of free-tropospheric humidity $q_0$, for SST = 300 K. Reference free-tropospheric profiles are shown by gray lines.

and can reach large values (up to 100% cloud fraction and 100 g m$^{-2}$ LWP) because of the stratus deck that develops at the top of the shallow cumulus layer.

Figure 9 shows the LES subcloud conserved variables, cloud base and inversion top, ABL growth rate, and surface turbulent fluxes as a function of $q_0$. As in Fig. 3, LES stationary states are indicated by filled circles and almost stationary variables in the unstable case are indicated by open circles. The stationary ABL depth increases with $q_0$ (Fig. 9a), and the ABL growth is slow for $q_0 = 10$ g kg$^{-1}$. The well-mixed temperature is not sensitive to $q_0$ since it is tied to the SST (Fig. 9c). The well-mixed humidity increases linearly with increasing free-tropospheric humidity, by about 20% of the increase in $q_0$ (Fig. 9d). The surface sensible heat flux is hardly sensitive to $q_0$ (Fig. 9e). On the contrary, changes in $q_0$ cause large changes in the surface latent heat flux

(Fig. 9f): moistening the subcloud layer by increasing $q_0$ reduces evaporation. The ABL deepening with increasing $q_0$ and the instability of the layer in the case $q_0 = 10$ g kg$^{-1}$ are not associated with increased surface buoyancy flux as in the case of an increase of SST. Rather, the deepening of the ABL is due to increased entrainment at the cloud top associated with increased condensation, since the ventilation of the ABL by the subsidence is less and less efficient as the free troposphere gets moister.

### d. Sensitivity of a well-mixed ABL to free-tropospheric humidity

We perform LES for an SST of 296 K and varying free-tropospheric specific humidity, from 2 to 14 g kg$^{-1}$, with a 2 g kg$^{-1}$ step. In all cases, the LES reaches a stationary state. For $q_0 \leq 8$ g kg$^{-1}$, this steady state is a well-mixed
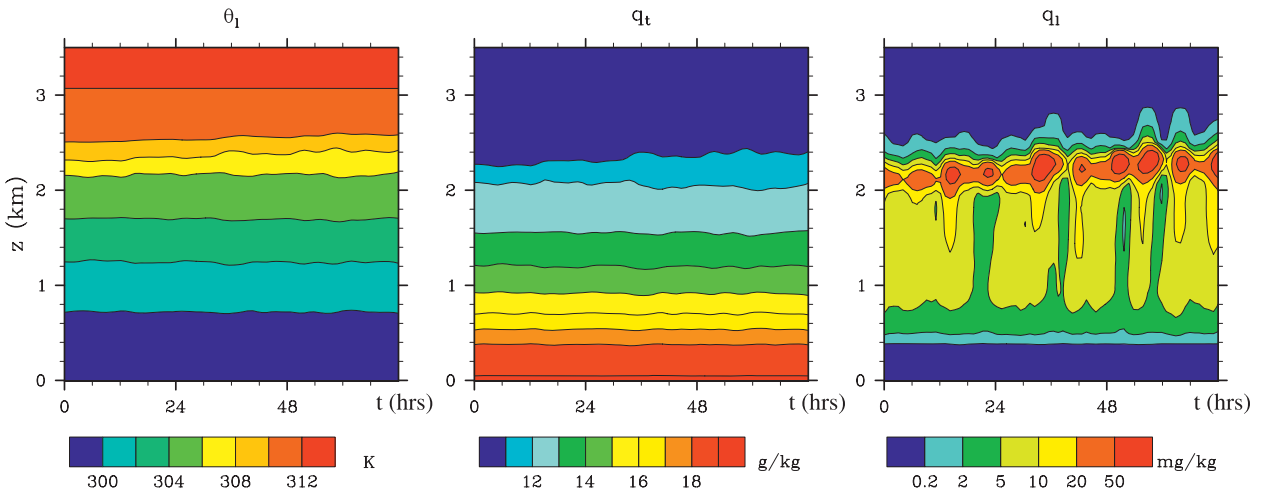


FIG. 7. Time evolution of 3-h-running-average (left) liquid water potential temperature, (middle) total water mixing ratio, and (right) liquid water mixing ratio for $q_0 = 10$ g kg$^{-1}$ (days 2–4).
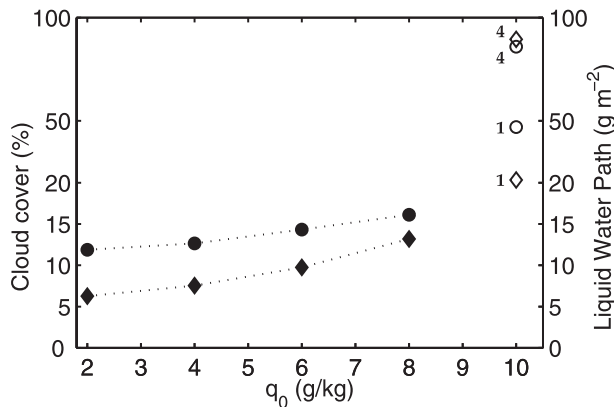
FIG. 8. Sensitivity of the stationary mean cloud fraction (circles) and liquid water path (diamonds) to the free-tropospheric humidity $q_0$, for SST = 300 K. Stationary means are shown by filled markers and selected daily averages are shown by open markers for the unstable case (days 1 and 4 of integration are indicated by "1" and "4" labels).

ABL that is cloud-free for $q_0 \leq 4$ g kg$^{-1}$ and capped by cumulus humilis for $q_0 \geq 6$ g kg$^{-1}$. For $q_0 \geq 10$ g kg$^{-1}$, stratocumuli develop in the cloud layer with increasing $q_0$, and the cloud layer progressively decouples from the subcloud layer. Figure 10 shows the mean profiles of the thermodynamic variables in stationary state. The ABL moistens with increasing $q_0$, but in small proportion compared to the changes in $q_0$. The stationary ABL depth is somewhat shallower for moister free troposphere in the well-mixed regime (for $q_0 \leq 8$ g kg$^{-1}$), whereas it deepens with increasing free-tropospheric humidity in the decoupled, stratus-capped regime (for $q_0 \geq 10$ g kg$^{-1}$). The liquid water ratio increases considerably in the decoupled regime, up to two orders of magnitude larger than in the well-mixed regime.

Figure 11 shows the sensitivity of the stationary cloud fraction and liquid water path to $q_0$. Both the cloud fraction and LWP increase exponentially with free-tropospheric humidity. The cloud fraction and LWP are small in the well-mixed regime (below 5% and 1 g m$^{-2}$), and they increase to large values in the decoupled regime with the development of a stratocumulus deck (up to 100% cloud fraction and 100 g m$^{-2}$ LWP for $q_0 = 14$ g kg$^{-1}$).

Figure 12 shows the LES stationary well-mixed variables, ABL depth, ABL growth rate, and surface turbulent fluxes as a function of $q_0$. In the well-mixed regime, $h$ decreases with increasing $q_0$; as the layer becomes decoupled, $h$ starts increasing with $q_0$ (Fig. 12a). There is no unstable case in this sensitivity experiment for the parameter range we consider (Fig. 12b). The well-mixed humidity $q_M$ increases almost linearly with increasing free-tropospheric humidity, by about 15% of the increase in $q_0$ (Fig. 12d). The surface sensible heat flux is small in

all cases; it increases (decreases) with increasing $q_0$ in the well-mixed (decoupled) regime (Fig. 12e), in keeping with a small sensitivity of $\theta_M$ (Fig. 12c). As in the ShCu case, changes in $q_0$ cause large changes in the surface latent heat flux (Fig. 12f): moistening the subcloud layer by increasing $q_0$ reduces evaporation. This reduction in evaporation translates into a decrease in the surface buoyancy flux. This reduced buoyancy flux, together with an enhanced effective stability (i.e., the jump in buoyancy across the inversion) associated with the increase in free-tropospheric buoyancy, explains the shoaling of the ABL for increasing $q_0 \leq 8$ g kg$^{-1}$. For $q_0 > 8$ g kg$^{-1}$, the cloud fraction increases significantly with $q_0$ (Fig. 11) because the subsidence becomes increasingly ineffective at ventilating the ABL. A large cloud fraction causes a large entrainment at the top of the ABL because of strong cloud-top entrainment. In a stationary state, the entrainment equals the subsidence at the top of the inversion, which increases with ABL depth. For a very moist free troposphere ($q_0 > 8$ g kg$^{-1}$), the ABL deepens with increasing entrainment associated with increasing cloud fraction and $q_0$. The strong cloud-top entrainment can also explain the decoupling between the subcloud and cloud layers. The decoupling also reduces the effective stability and thus contributes to the deepening of the ABL.

## 4. Evaluation of the sensitivity of bulk models

In this section, we seek to illustrate how a set of LESs such as the one we described in the previous section can be used as a benchmark to evaluate simpler models or parameterizations of the ABL. Although the observed ABL is hardly ever stationary, it seems reasonable to expect simple parameterizations to be able to simulate the steady states similar to the stationary states of a more realistic—although imperfect—model such as a LES, because these steady states constrain the transients. We present results concerning a simple bulk model (called XLM) based on the mixing-line model first developed by Betts and Ridgway (1988, 1989); we reformulate it in terms of simple parameters and modify its closures to try to generalize its relevance. Note that the use of the mixing-line hypothesis in our model reduces to two very simple matching conditions that could be imposed independently from the physical assumption underlying the mixing-line hypothesis.

### a. Mixing-line model (XLM)

This model is based on the assumption that the diabatic sources and horizontal transport of conserved variables ($\theta_l$ and $q_t$) are small in front of the contributions from the turbulent mixing and vertical advection in a shallow convective ABL. The vertical profiles of the
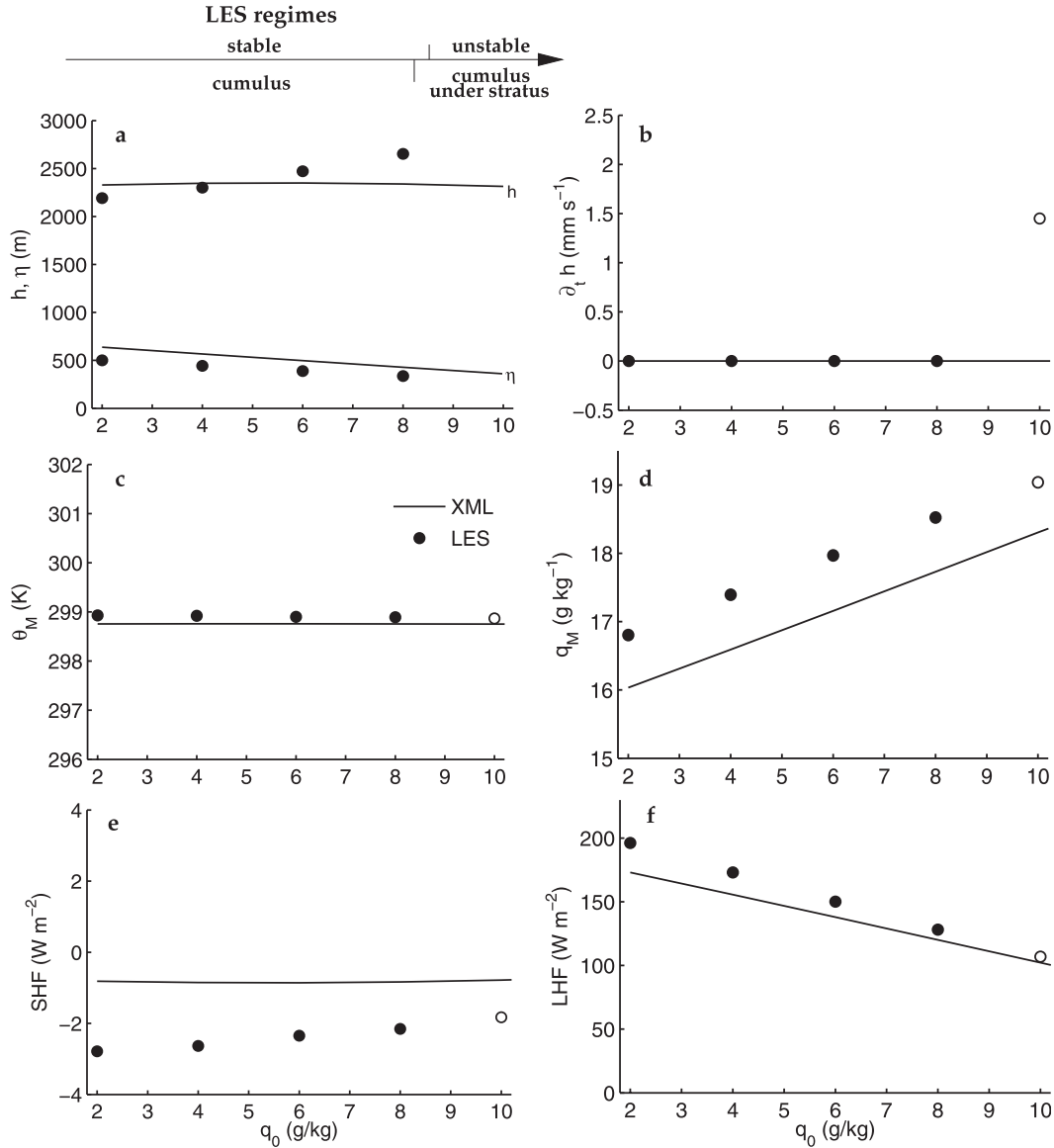
FIG. 9. Sensitivity to free-tropospheric humidity $q_0$ of (a) ABL depth $h$ and depth of the well-mixed layer $\eta$, (b) ABL growth, (c) well-mixed potential temperature, (d) well-mixed specific humidity, (e) surface sensible heat flux, and (f) surface latent heat flux, for SST = 300 K. LES stationary states are shown by filled circles, and almost-stationary variables from unstable LES cases are shown by open circles. Solid lines show the results from the bulk model XLM.

conserved variables follow a "mixing line" between the subcloud values and the values at the top of the inversion:

$$\phi = \phi_M[1 - f(z')] + f(z')\phi_{i^+}(h), \qquad (5)$$

where $\phi$ is a conserved variable ($\phi = \theta_l$ or $\phi = q_t$); $\phi_M$ is the subcloud, well-mixed value of $\phi$, and $\phi_{i^+}(h)$ is its value at the top of the inversion; and $f$ is the ratio of the air parcel that originated in the free troposphere. We use the normalized vertical coordinate $z' = (z - \eta)/(h - \eta)$,

with $h$ being the altitude of the top of the inversion at which the thermodynamic profiles merge with the reference free-tropospheric profiles, and $\eta$ the altitude of the top of the well-mixed layer. By construction, $f(0) = 0$ and $f(1) = 1$. This approach was originally designed for ShCu cases, with $\eta$ being the altitude of the cloud base. We can generalize it to cloud-free cases by considering that the mixing line can apply to an extended layer that includes both the cloud layer and the inversion layer in the ShCu cases, and just the inversion layer in the well-mixed
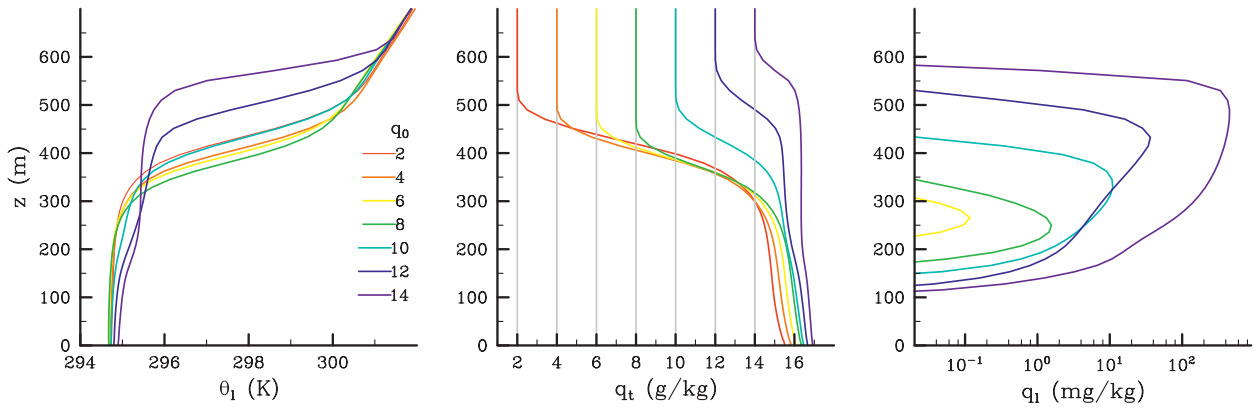
FIG. 10. Stationary mean profiles of (left) liquid water potential temperature, (middle) total water mixing ratio, and (right) liquid water mixing ratio for different values of free-tropospheric humidity $q_0$, for SST = 296 K. Reference free-tropospheric profiles are shown by gray lines.

cases. Hereafter we simply refer to this as the upper mixing layer. This is consistent with our analysis of the LES using criterion in Eq. (4).

The local budget of energy and water can be written

$$\partial_t \phi = -w(z)\partial_z \phi - \partial_z F^\phi + \sigma_\phi, \qquad (6)$$

where $F^\phi$ is the turbulent flux and $\sigma_\phi$ combines the diabatic source and horizontal transport of $\phi$. Using the mixing-line hypothesis, it can be rewritten as

$$\partial_t \phi = -w(z)[\phi_{i^+}(h) - \phi_M]\partial_z f(z) - \partial_z F^\phi + \sigma_\phi, \quad (7)$$

and the bulk budget can be expressed as

$$h \cdot \partial_t \langle \phi \rangle + \partial_t h \cdot [\langle \phi \rangle - \phi_{i^+}(h)]$$
$$= -w(h)\gamma[\phi_{i^+}(h) - \phi_M] + F_0^\phi + \langle \sigma_\phi \rangle h, \qquad (8)$$

where $\langle \phi \rangle$ is the vertical average of $\phi$ over the ABL (i.e., from the surface to the top of the inversion),

$$\langle \phi \rangle = \int_0^h \phi(z)\frac{dz}{h} = \phi_M + \alpha \left(1 - \frac{\eta}{h}\right)[\phi_{i^+}(h) - \phi_M]; $$

$\alpha$ and $\gamma$ introduce two parameters that are integrals of $f$:

$$\alpha = \int_0^1 f(z')\, dz' \qquad (9)$$

and

$$\gamma = \int_\eta^h \partial_z f \frac{w(z)}{w(h)}\, dz. \qquad (10)$$

The budget of the well-mixed layer can be obtained by integrating Eq. (6) between the surface and the top of the well-mixed layer:

$$\eta \cdot \partial_t \phi_M = F_0^\phi - F^\phi(\eta) + \langle \sigma_\phi \rangle_M \eta, \qquad (11)$$

where $\langle \sigma_\phi \rangle_M$ is the vertical average of $\sigma_\phi$ over the well-mixed layer.

The turbulent surface fluxes are parameterized using bulk formulas:

$$F_0^\phi = w_s(\phi_s - \phi_M),$$

where $w_s = C_D U$, where $C_D = 1.2 \times 10^{-3}$ is a drag coefficient and $U$ is the geostrophic wind. Also, $\phi_s$ is the equivalent surface value of $\phi$; $q_s = q^*(T_s)$ is the saturated mixing ratio at the surface pressure $p_s$ and sea surface temperature $T_s$; and $\theta_s = T_s(p_0/p_s)^k$, with $p_0$ being the reference pressure.



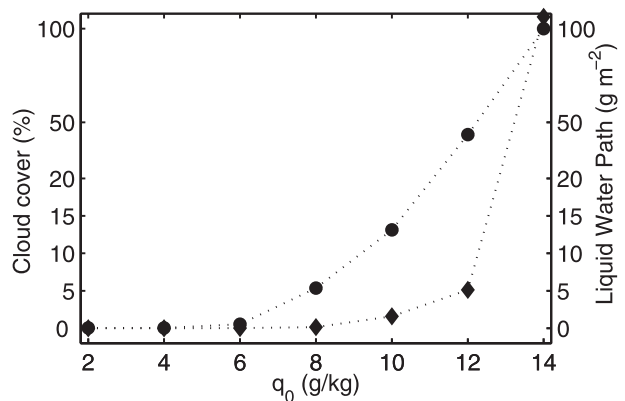FIG. 11. Sensitivity of the stationary mean cloud fraction (circles) and liquid water path (diamonds) to the free-tropospheric humidity $q_0$, for SST = 296 K.
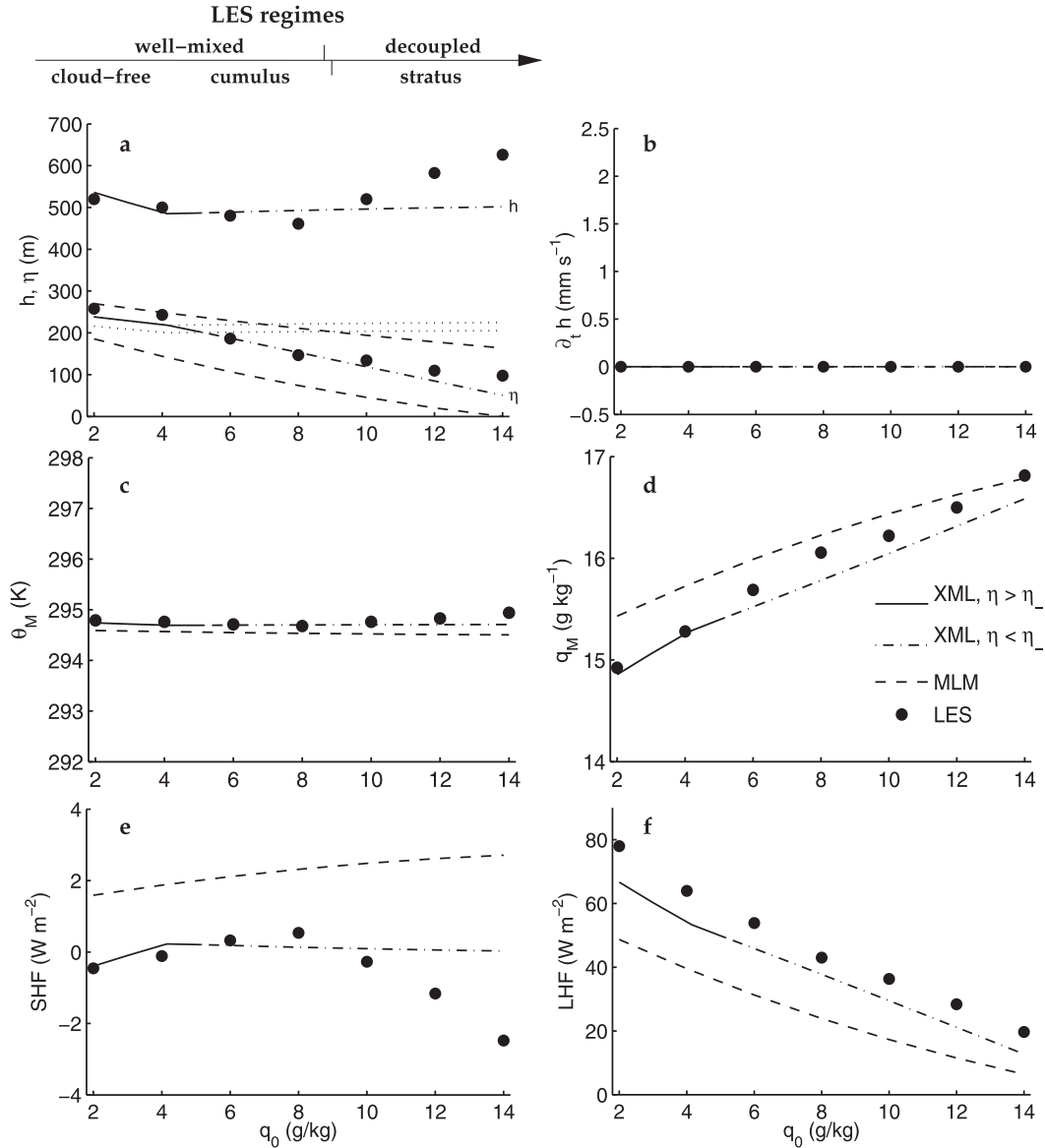
FIG. 12. Sensitivity to free-tropospheric humidity $q_0$ of (a) ABL depth $h$ and depth of the well-mixed layer $\eta$, (b) ABL growth, (c) well-mixed potential temperature, (d) well-mixed specific humidity, (e) surface sensible heat flux, and (f) surface latent heat flux, for SST = 296 K. LES stationary states are shown by filled circles. Solid lines show the XLM results with consistent altitude of the top of the well-mixed layer ($\eta \geq \eta^-$); dash-dotted lines show the XLM results with inconsistent $\eta$ ($<\eta^-$). In (a), dotted lines show the bounds $\eta^-$ and $\eta^+$ on $\eta$, and dashed lines show the MLM ABL depth $h$ and cloud base (LCL).

Two closures are necessary to close the mathematical system. One closure is to consider the buoyancy flux at the top of the well-mixed layer proportional to the surface buoyancy flux:

$$F^v(\eta) = -kF_0^v, \qquad (12)$$

where $F^v$ is the buoyancy flux and $k = 0.2$ is the closure parameter. This closure was established empirically

(Deardorff et al. 1969) and used in the first bulk (mixed-layer) models of the boundary layer (Lilly 1968; Deardorff 1972), as well as subsequent bulk models of the shallow cumulus boundary layer (Betts and Ridgway 1988; Betts and Ridgway 1989). Computing $k$ from our LESs yield values close to 0.2 as well (not shown). This closure can be combined with the water and energy budgets of the well-mixed layer [Eq. (11)] to write the well-mixed-layer budget of buoyancy:

$$\eta \cdot \partial_t b_M = (1 + k)F_0^v + \langle \sigma_b \rangle_M \eta, \qquad (13)$$

where $b_M = \theta_M(1 + \epsilon_1 q_M)$ is the subcloud-layer buoyancy and $\sigma_b = \sigma_\theta(1 + \epsilon_1 q_M) + \theta_M \epsilon_1 \sigma_q$ is the horizontal transport/diabatic source of buoyancy. The surface buoyancy flux can be written $F_0^v = F_0^\theta(1 + \epsilon_1 q_M) + \theta_M \epsilon_1 F_0^q$, where $\epsilon_1 = R_v/R_d - 1$, with $R_d$ $(R_v)$ being the gas constant of dry air (water wapor).

The other usual closure used in bulk models is to set the top of the well-mixed layer at the lifting condensation level (LCL). Here, we want to be able to simulate cloud-free ABLs as well as cloudy ones so that we compute a maximum $\eta$ based on geometrical considerations on the mixing-line function $f$. If the LCL is below this maximum, the ABL is considered cloudy and the $\eta$ is set to the LCL; otherwise, $\eta$ is set to its maximum and the ABL is considered cloud free. Bounds on $\eta$ can be deduced from the constraints on $f$: $f$ belongs to a family of functions monotonically increasing from 0 to 1 between $z' = 0$ and $z' = 1$, and with a vertical average of $\alpha$. Within this family we can pick two extreme functions: $f_-$, which corresponds to splitting the upper mixing layer in two homogeneous layers, one with the thermodynamical properties of the well-mixed layer and the other with the properties of the top of the inversion; and $f_+$, which corresponds to a homogeneous upper mixing layer. Using the expression of $\gamma$ [Eq. (11)], these functions provide bounds $\eta^-$ and $\eta^+$ on $\eta$. Details on the derivations of these bounds are given in appendix B. They can be expressed as functions of $h$ and the model parameters:

$$\eta^- = h - \frac{z_w}{\alpha} \ln[\gamma + (1 - \gamma)e^{h/z_w}], \qquad (14a)$$

$$\eta^+ = h - z_w \ln\left[1 + \frac{1 - \gamma}{\alpha}(e^{h/z_w} - 1)\right]. \qquad (14b)$$

The closure used in our formulation of the XLM considers that the top of the well-mixed layer $\eta$ is at the LCL if this level is below the upper bound $\eta^+$ (cloudy case), and it is otherwise $\eta^+$ (cloud-free case):

if $\quad q_M \geq q^*[T_{WM}(\eta^+), p_{WM}(\eta^+)], \quad$ then

$q_M = q^*[T_{WM}(\eta), p_{WM}(\eta)], \qquad (15a)$

otherwise, $\quad \eta = \eta^+, \qquad (15b)$

where $T$ and $p$ are the temperature and pressure. Also, $T_{WM}(z)$ and $p_{WM}(z)$ are the well-mixed profiles of temperature and pressure, which can be computed from surface values: $T_{WM}(z) = T_0 - gz/c_p$ and $p_{WM}(z) = p_s(1 - gz/c_p T_0)^{1/\kappa}$, where $c_i$ is the heat capacity of air and $T_0$ the surface temperature: $T_0 = \theta_M(p_s/p_0)^\kappa$.

To compare our XLM to the LES, we set the horizontal transport/diabatic terms to constants,

$$\sigma_\theta = -R \quad \text{and} \quad \sigma_q = 0,$$

and the large-scale vertical wind speed $w(z)$ following Eq. (1). The bulk water budget can then be written as

$$h \cdot \partial_t \langle q_t \rangle + \partial_t h \cdot (\langle q_t \rangle - q_0) = w_h \gamma(q_0 - q_M) + w_s(q_s - q_M), \qquad (16)$$

and the bulk energy budget as

$$h \cdot \partial_t \langle \theta_l \rangle + \partial_t h \cdot [\langle \theta_l \rangle - \theta_{i^+}(h)] = w_h \gamma[\theta_{i^+}(h) - \theta_M] + w_s(\theta_s - \theta_M) - Rh, \qquad (17)$$

with

$$w_h = -w(h) = w_0 \cdot (1 - e^{-h/z_w}).$$

And the well-mixed-layer buoyancy budget (14) can be rewritten as

$$\eta \cdot \partial_t(\theta_M + \psi q_M) = (1 + k)w_s[\theta_s - \theta_M + \psi(q_s - q_M)] - R\eta, \qquad (18)$$

with $\psi = \epsilon_1 \theta_M(1 + \epsilon_1 q_M)^{-1}$.

Once the parameters $\alpha$ and $\gamma$ are set, the budgets in Eqs. (16), (17), and (18) associated with the closure in Eqs. (15) constitute a closed mathematical system.

Note that the classical mixed-layer model (MLM; Lilly 1968; Deardorff 1972) corresponds to the same equations as our XLM with $\alpha = 0$, $\gamma = 1$, and $\eta$ set to $h$ instead of using the closures in Eqs. (15). The MLM ABL is considered cloudy if the LCL is below $h$, and cloud-free otherwise. We will use this MLM model as well as our XLM in our sensitivity studies to compare skill between bulk models.

### b. Parameter evaluation

In general, the parameters $\alpha$ and $\gamma$ can be prescribed by making some assumptions on the upper-mixing-layer profile. Here, we choose to use our set of LES to compute these parameters. In doing so, we can on one hand evaluate the validity of the mixing-line simplification; on the other hand, we constrain our XLM to resemble the LES, so that the relevance of the evaluation of the XLM is weakened. But here this exercise is intended more as an illustration of our evaluation strategy than an actual validation.

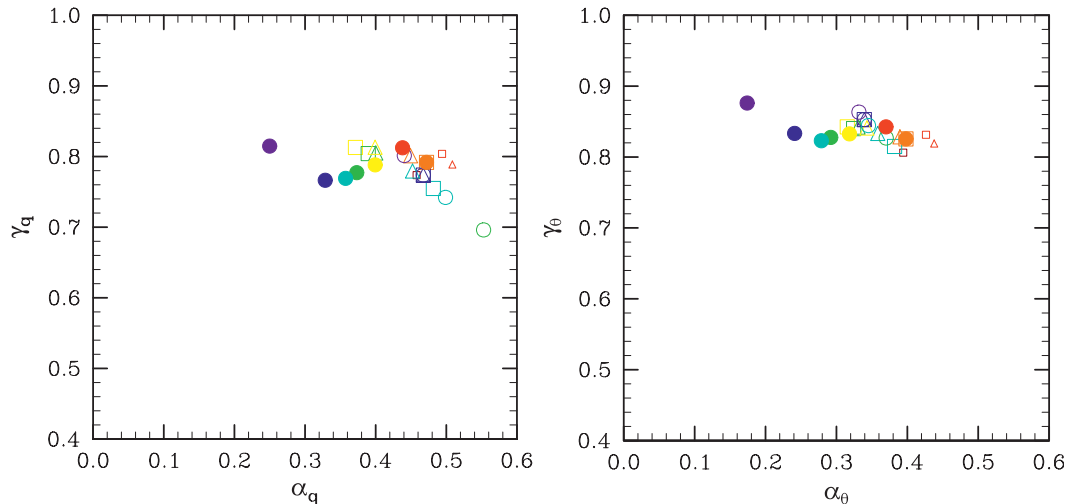We can compute two evaluations of $f$ ($f_\theta$ and $f_q$) for each LES, using $\phi = \theta_l$ or $\phi = q_t$:

FIG. 13. Scatterplots of $\gamma_q$ and $\gamma_\theta$ as functions of $\alpha_q$ and $\alpha_\theta$, evaluated from the LES stationary states. Cases with varying SST are shown by squares, cases with varying $\theta_r$ are shown by triangles, cases with SST = 300 K and varying $q_0$ are shown by open circles, and cases with SST = 296 K and varying $q_0$ are shown by filled circles. The colors follow the legends in Figs. 1, 5, 6, and 10. Large markers indicate cloudy ABLs and small markers cloud-free ABLs.

$$f_\phi = \frac{\phi(z) - \phi_M}{\phi_{i^+}(h) - \phi_M}. \qquad (19)$$

Equation (19), together with Eqs. (9) and (10), yields two evaluations $\alpha_\theta$ and $\alpha_q$ ($\gamma_\theta$ and $\gamma_q$) of parameter $\alpha$ ($\gamma$) for each LES. Figure 13 shows these evaluations for each LES stationary state. Note that Fig. 13 only shows part of the possible range for $\alpha$ and $\gamma$, which are by definition between 0 and 1. The scatterplots show that the mixing-line hypothesis is reasonable, namely that (i) the evaluations of $\alpha$ and $\gamma$ are similar using $\theta_l$ and $q_t$, and that (ii) they are similar from one LES to the other. In more details, the sensitivity to free-tropospheric humidity departs slightly from (i) and (ii) for both the ShCu and well-mixed regimes. For the well-mixed regime, the spread in the values of $\alpha_q$ and $\alpha_\theta$ result in large part from the decoupling between subcloud and cloud layers. The average $\alpha_\theta$ and $\alpha_q$ values over all simulations are 0.34 and 0.43, respectively. The average $\gamma_\theta$ and $\gamma_q$ values over all simulations are 0.78 and 0.83, respectively. Overall, $\alpha = 0.4$ and $\gamma = 0.8$ are reasonable choices for our XLM parameters. These are the values we use in the next section.

## c. Evaluation of the model sensitivity

We study the sensitivity of our XLM to the underlying SST and the sensitivity of the ShCu case ($T_s = 300$ K) and well-mixed case ($T_s = 296$ K) to the free-tropospheric humidity $q_0$, all other boundary conditions and forcings being identical to our LES.

Overall, the XLM fairly reproduces the LES sensitivity to SST changes. For SSTs cooler than a threshold

$T_s^u \approx 300.1$ K, the XLM reaches an equilibrum that is cloud free for SSTs cooler than a threshold $T_s^c \approx 296.7$ K and cloudy for warmer SSTs. For SSTs warmer than $T_s^u$, the XLM does not reach a steady state and simulates a growing cloudy ABL. In these unstable cases, the turbulent surface fluxes and well-mixed humidity and temperature are almost steady. Figure 3 shows the model variables in the stable steady states and the almost steady variables in the unstable cases. The sensitivity of the XLM is similar to that of the LES in terms of ABL depth (Figs. 3a,b): the XLM captures the transition from a cloud-free, well-mixed ABL to unstable, cloudy ABL with SST thresholds similar to the LES thresholds. The XML exhibits two small biases: it seems to underestimate the ABL depth at low SSTs and the ABL growth for warm SSTs. The sensitivity of $\theta_M$ is similar in the LES and XLM (Fig. 3c), but the sensitivity of $q_M$ is underestimated by the XLM (Fig. 3d); in particular, the XLM underestimates $q_M$ for warm SSTs. Despite this discrepancy in near-surface humidity, the LHF exhibits similar sensitivities in the XLM and LES (Fig. 3f). This suggests that the bulk formula used in the XLM compensates for the difference in $q_M$ between LES and XLM, and that the LES LHF is not directly proportional to the difference between $q^*(T_s)$ and $q_M$; some other factors such as subgrid wind (i.e., gustiness) or surface-layer gradients have a strong impact on the LHF. The sensitivity of the SHF to SST is not as nonlinear in the XLM as in the LES (Fig. 3e), but considering the small amplitude of the SHF, this discrepancy is not very significant.

The sensitivity of the XLM to the free-tropospheric temperature is also fairly similar to the LES sensitivity (not shown): a 1-K increase in $\theta_r$ is roughly equivalent to a 1-K decrease in SST. The main differences are a better estimation of $q_M$ and its sensitivity, and an underestimation by about 2 K of the $\theta_r$ threshold for the transition between cloudy and cloud-free ABL.

As a comparison, we show in Fig. 3 the same sensitivity experiment conducted with the MLM. This model does not reproduce the LES results at all, even for cloud-free, well-mixed ABLs for which it is usually thought to be better suited than the XLM. The MLM considerably underestimates the ABL depth and evaporation, fails to predict the instability of the ABL for warm SSTs, and simulates a cloudy ABL even for cool SSTs (see Fig. 3a).

Figure 9 shows the XLM sensitivity of the ShCu case to $q_0$. For the range of $q_0$ studied here, the XLM reaches a steady state. The XLM does not simulate the increase in ABL depth with increasing $q_0$ and does not reproduce the instability of the stratus-capped ABL (Figs. 9a,b). Further experiments showed that this failure cannot be remediated by allowing $\alpha$ and $\gamma$ to vary linearly with $q_0$ as suggested by Fig. 13 or by allowing $\alpha_\theta$ ($\gamma_\theta$) to differ from $\alpha_q$ ($\gamma_q$) (not shown). The failure to capture the ABL sensitivity to free-tropospheric humidity results most likely from the inability of the XLM to simulate the entrainment processes at play in the LES at the top of the stratus; the instability produced by these entrainment processes is not powered by the surface buoyancy flux, unlike in the case of the sensitivity to SST and free-tropospheric temperature. The XLM captures the LES sensitivity of the subcloud thermodynamic variables $\theta_M$ and $q_M$, although $q_M$ is systematically underestimated (Figs. 9c,d). The XLM also exhibits a small bias for the sensitivity of turbulent surface fluxes, although the SHF sensitivity is not very significant (Fig. 9e). The XLM generally underestimates the LHF—despite the underestimation of $q_M$—and its decrease with increasing $q_0$ (Fig. 9f). This shows again that LES LHF is not directly proportional to the difference between $q^*(T_s)$ and $q_M$. Possible reasons for this are mentioned hereabove.

Figure 12 shows the XLM sensitivity of the well-mixed case to $q_0$. The XLM reaches a steady state over the range of $q_0$ studied here. This steady state is cloud free for a free troposphere dryer than a threshold $q_0^c \approx 4.2 \, \text{g kg}^{-1}$ and cloudy for a moister free troposphere. This is very similar to the LES. But for a free troposphere moister than a threshold $q_0^i \approx 5.2 \, \text{g kg}^{-1}$, the XLM steady state is not self-consistent since $\eta$ is smaller than its geometrically determined lower bound $\eta^-$. In other words, this steady state is inconsistent with the mixing-line assumptions. This is not completely unexpected, since the LESs with

an SST of 296 K and varying $q_0$ exhibit a significant spread in $\alpha$ (see Fig. 13), and $\eta^-$ is quite sensitive to $\alpha$, as can be infered from Eq. (15a). Nevertheless, the XLM steady state, self-consistent or not, captures some of the sensitivity of the LES to the free-tropospheric humidity. The well-mixed potential temperature is tied to the SST (Fig. 12c), and the well-mixed humidity increases with increasing $q_0$ (Fig. 12d). The XLM does not quite capture the nonlinearity of the SHF sensitivity to $q_0$, but here again the SHF is very small (Fig. 12e). The XLM slightly underestimates the LHF for large $q_0$ but it does capture its overall sensitivity (Fig. 12f). Although the XLM appears to capture the sensitivity of the well-mixed ABL depth to free-tropospheric humidity for low $q_0$, it seems unable to capture the increase in $h$ for large $q_0$. This suggests again that the XLM cannot reproduce the cloud-top entrainment processes that are particularly active for large cloud fractions (Fig. 12a). On the other hand, because the subcloud conserved variable are well simulated by the XLM, the cloud base and its sensitivity to $q_0$ are faithfully reproduced.

We perform the same sensitivity study with the MLM that is considered well suited to simulate well-mixed ABLs. Figure 12 shows that the MLM does not reproduce the LES results any better than the XLM, even in this well-mixed case: it simulates a too shallow, systematically cloudy ABL, and even fog for very high $q_0$.

In summary, the XLM does reproduce the LES results for the sensitivity of ABL to SST (and free-tropospheric temperature), and in particular the transition from well-mixed ABL to stable ShCu ABL and to growing ShCu ABL. It also reproduces the sensitivity of the well-mixed ABL to $q_0$ around the control well-mixed case. Considering the simplicity of the XLM, it is surprisingly skilled at reproducing the LES sensitivities. In all cases, it fares better than the MLM. But it appears unable to capture the sensitivity of the ShCu ABL to the free-tropospheric humidity and the sensitivity of the well-mixed ABL to large $q_0$. Both shortcomings result in part from the XLM's inability to reproduce the cloud-top entrainment processes, but the second shortcoming also shows the conceptual limit of the XLM, because the XLM steady state becomes inconsistent with its own formulation.

This model evaluation using our LES dataset can be conducted with any other ABL model or parameterization.

### d. Transition from stable to unstable ShCu ABL

Reproducing this transition is one success of the XLM at reproducing the LES results. We can try to use this simple model to understand the dynamics of this transition. At equilibrium, the water and energy budgets in

Eqs. (16) and (17) can be rewritten so that the subcloud thermodynamic variables can be expressed as functions of the depth of the ABL:

$$q_M = Q(h) = \frac{w_h \gamma q_0 + w_s q_s}{w_h \gamma + w_s} \quad \text{and}$$

$$\theta_M = \Theta(h) = \frac{w_h \gamma \theta_{i^+}(h) + w_s \theta_s - Rh}{w_h \gamma + w_s}.$$

The well-mixed-layer buoyancy budget in Eq. (18) can be used to express $\eta$ as a function of $h$:

$$\eta = H(h) = (1 + k)\frac{w_s}{R}\bigg\{\theta_s - \Theta(h)$$

$$+ \frac{\epsilon_1 \Theta(h)}{1 + \epsilon_1 Q(h)} \cdot [q_s - Q(h)]\bigg\}.$$

Finally, the closure in Eq. (15a) allows us to write the condition for steady state as a single equation in $F(h) = 0$:

if    $Q(h) \geq Q^*[\eta^+(h)],$    then

$F(h) = Q(h) - Q^*[H(h)];$

otherwise    $F(h) = Q^*[\eta^+(h)] - Q^*[H(h)],$

where $Q^*(z) = q^*\{T_{WM}[z, \Theta(h)], p_{WM}[z, \Theta(h)]\}$ is the saturation water vapor mixing ratio at the temperature and pressure following a dry adiabat from the surface. The second part of this equation could be simply expressed $F(h) = \eta^+(h) - H(h)$, but the above formulation ensures the continuity of the function $F$ at transitions between cloudy and cloud-free conditions.

This function $F$ is plotted in Fig. 14 for different values of SST, with all other forcings as in the ShCu control case. It appears that for SSTs cooler than $T_s^c$, $F$ has three zeros: one for $h_0 = 0$ (not shown), and two for $h_2 > h_1 > 0$. The equilibrium at $h = h_1$ (circles in Fig. 14) is stable and it is the equilibrium discussed in the previous section. Time integrations using the prognostic XLM show that the equilibria for $h = 0$ or $h = h_2$ are unstable (not shown). For SSTs warmer than $T_s^c$, $F$ has only one unstable equilibrium for $h_0 = 0$: whatever the initial conditions, the ABL grows indefinitely. This shows that the transition between stable and unstable ABL is associated with a saddle-node bifurcation in the XLM. The LES yields an ever-growing ABL for warm SSTs; this suggests that the transition might also result from a saddle-node bifurcation in the LES.

## 5. Summary and discussion

We have studied the sensitivity of the UCLA LES stationary state to large-scale conditions of temperature and humidity, from shallow cumulus control conditions
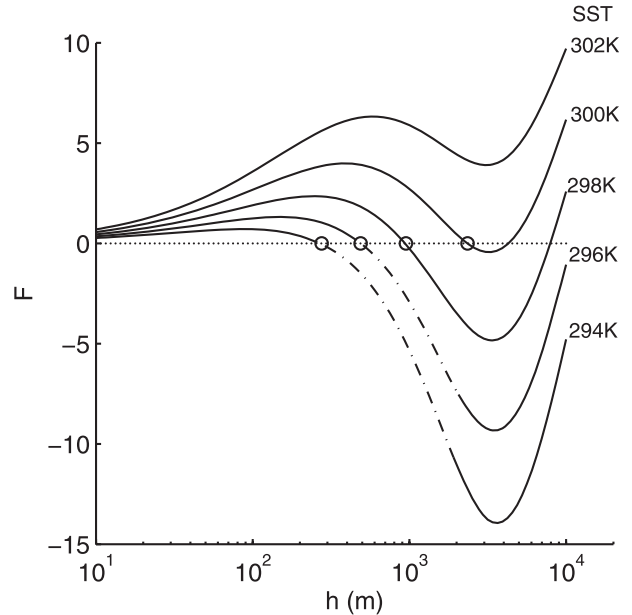


FIG. 14. Function $F(h)$ for varying SST. Solid lines indicate that the closure in Eq. (15a) is used (cloudy ABL), and dash-dotted lines indicate that the closure in Eq. (15b) is used (cloud-free ABL). Circles indicate stable equilibria of the XLM.

similar to the BOMEX case and well-mixed control conditions with a lower SST. For increasing SST or decreasing free-tropospheric temperature, our LES simulates a transition from a cloud-free, well-mixed ABL, through cumulus-capped, well-mixed ABL and a stable shallow cumulus ABL, to an ever-growing shallow cumulus ABL. For increasing free-tropospheric humidity, our LES simulates a transition from a stable shallow cumulus ABL, through a stable cumulus-under-stratus ABL, to an unstable cumulus-under-stratus ABL if the SST is warm (300 K). If the SST is cool (296 K), our LES simulates a transition from a cloud-free, well-mixed ABL to a well-mixed ABL capped by small cumuli to a decoupled ABL with a large stratiform cloud cover.

This set of experiments can be used as a benchmark to evaluate simpler models. To illustrate this approach, we have used our LES results to evaluate the skill of two simple bulk models: a bulk model (XLM) inspired from the mixing-line model (Betts and Ridgway 1988; Betts and Ridgway 1989) and a basic mixed-layer model (MLM). In the XLM, the mixing-line hypothesis is applied in a weak, integral form that yields two bulk parameters $\alpha$ and $\gamma$ describing the vertical structure of the ABL; the XLM could be defined independently from the mixing-line hypothesis by imposing these two parameters. An analysis of our LESs shows that the two bulk parameters $\alpha$ and $\gamma$ can be determined using the dataset built up from our simulations. The XLM performs systematically better than our basic MLM, even for
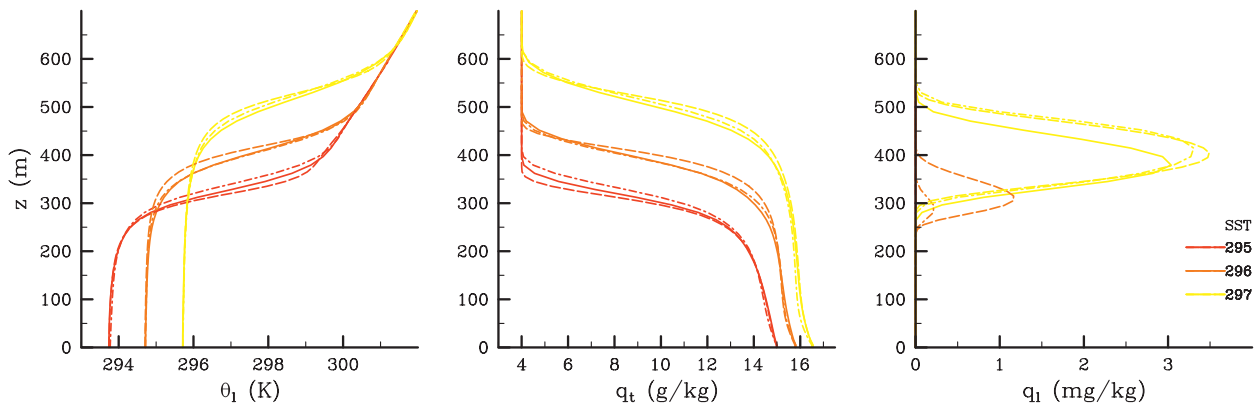
FIG. A1. Stationary mean profiles of (left) liquid water potential temperature, (middle) total water mixing ratio, and (right) liquid water mixing ratio for different values of SST. Solid lines indicate our reference resolution, dash-dotted lines indicate double horizontal resolution (HR), and dashed lines indicate doubled horizontal resolution and uniform 10-m vertical resolution (Z&HR).

well-mixed ABLs. This might result from the combination of closure in Eq. (12) on the buoyancy flux at the top of the well-mixed layer and the infinitely thin inversion layer in our MLM: Uchida et al. (2010) have shown that an MLM with a different closure can reproduce an LES sensitivity in the well-mixed regime. But this difference in skill might also be specific to the range of large-scale conditions considered here.

The XLM is skillfull at reproducing the LES sensitivity to SST and free-tropospheric temperature but it is less successful at reproducing the sensitivity of the ShCu and well-mixed ABLs to free-tropospheric humidity. The XLM predicts the instability of the ShCu ABL for warm SSTs associated with a saddle-node bifurcation, with a threshold SST similar to that of the LES, but not the instability of the cumulus-under-stratus ABL for a moist free troposphere.

We intend to use this benchmark to evaluate the sensitivity of GCM parameterizations. Whether commonly used parameterizations can reproduce the sensitivity of the stationary ABL to the large-scale conditions is unclear but we would hope that these parameterizations perform at least as well as the bulk XLM. Part of the XLM skill relies on the choice of parameters $\alpha$ and $\gamma$ that is based on the LES results; similarly, the LES dataset might be useful to constrain the key parameters of GCM parameterizations.

It seems interesting to complete the present study by experiments exploring the sensitivity of the LES to the large-scale forcing (subsidence and radiative cooling) to extend the benchmarking dataset and better understand the different LES regimes.

One limit of our validation approach is the constraint of stationarity: large-scale conditions change on synoptic scales and the extent to which the observed ABL ever reaches a quasi-equilibrium with the large-scale forcing

is unclear. But one can consider that the ABL time evolution can be described at first order by a relaxation toward the stationary state corresponding to the instantaneous large-scale conditions. To simulate correctly (i.e., without compensating errors) this relaxation, it is a necessary condition to simulate the correct stationary state, even if this steady state is never reached under more realistic conditions.

## APPENDIX A

### LES Sensitivity to Resolution

We choose to test the sensitivity of three cases around the transition between cloud-free and cloudy well-mixed ABL, with SSTs from 295 to 297 K. We conducted two additional simulations for each SST, one with double (25 m) horizontal resolution (resolution HR), and another with both double horizontal resolution and uniform 10-m vertical resolution (resolution Z&HR). Note that in our standard setup the vertical resolution is 10 m at the surface and increases by 2% at each level, so that this resolution is about 20 m at 500 m of altitude. Figure A1 shows the stationary profiles of the thermodynamic variables of all these experiments. It appears that the increase in resolution sharpens the inversion, with a dominant impact of the vertical resolution, but the profiles of the conserved variables are fairly robust. It is

TABLE A1. Sensitivity of the cloud fraction to the resolution.

| SST (K) | Cloud fraction (%) | | |
|---|---|---|---|
| | Standard | HR | Z&HR |
| 295 | 0 | 0 | 0 |
| 296 | 0.03 | 0.7 | 3.8 |
| 297 | 7.2 | 7.8 | 7.8 |

different for the liquid water: while the profiles of $q_l$ are not very sensitive to the resolution in the cases away from the transition (for SSTs of 295 and 297 K), the case at the transition (with an SST of 296 K) becomes cloudy when the resolution is increased, with a liquid water ratio up to 1 mg kg$^{-1}$ for the case with increased resolution in both the vertical and the horizontal.

The cloud fraction follows the same pattern, as shown in Table A1: it is not very sensitive for cases away from the transition and much more sensitive for cases near the transition.

These experiments show that the exact location of the transition is sensitive to the resolution, but only by a few tenths of degrees. We can expect the general behavior of the LES to be robust in terms of sensitivity, even if the SST thresholds between regimes are somewhat sensitive.

## APPENDIX B

### Bounds on $\eta$

Here, we detail how the mixing-line hypothesis and the choice of parameters $\alpha$ and $\gamma$ constrain the altitude $\eta$ of the top of the well-mixed layer through simple geometrical considerations.

The function $f$ defining the mixing line is part of the family of functions that is monotonically increasing with $z'$ and has an average of $\alpha$ between 0 and 1. Within this family, we can pick two extreme functions: $f_-$, which corresponds to splitting the upper mixing layer in two homogeneous layers, one with the thermodynamical properties of the well-mixed layer and the other with the properties of the top of the inversion; and $f_+$, which corresponds to a homogeneous layer with the average properties of the upper mixing layer:

$$f_-(z') = 0 \quad \text{for} \quad 0 < z' \le 1 - \alpha,$$
$$= 1 \quad \text{for} \quad 1 - \alpha < z' < 1; \quad \text{(B1)}$$

$$f_+(z') = \alpha \quad \text{for} \quad 0 < z' < 1. \quad \text{(B2)}$$

By definition, $f - f_-$ and $f - f_+$ averaged between 0 and 1 equal zero. Also by definition, $f - f_-$ changes sign from positive to negative at $z' = 1 - \alpha$. Note that $f - f_+$ also changes sign from negative to positive at a normalized
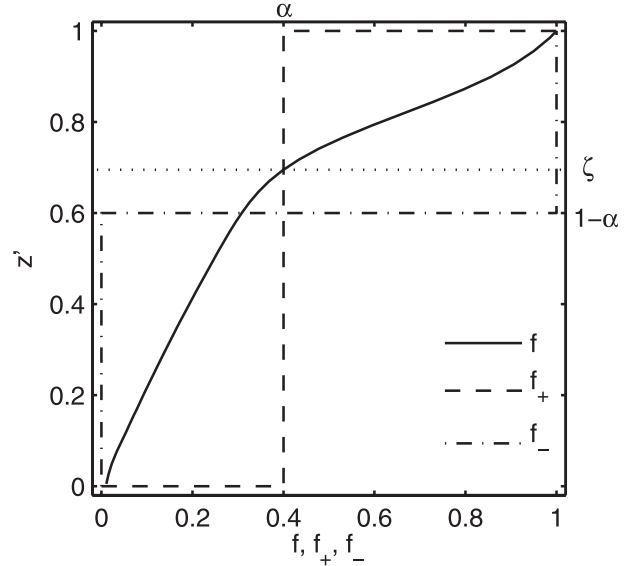


FIG. B1. Functions $f$, $f_+$, and $f_-$ as functions of the normalized altitude $z'$.

altitude hereafter noted $\zeta$. Figure B1 shows the functions $f_-$ and $f_+$, and an example of a function $f$.

The expression of $\gamma$ in Eq. (10) of the manuscript can be integrated by parts to yield

$$\gamma = 1 - \frac{\chi e^\chi}{e^{h/z_w} - 1} \mathcal{I}(\chi), \quad \text{(B3)}$$

with

$$\chi = \frac{h - \eta}{z_w} \quad \text{and} \quad \mathcal{I}(\chi) = \int_0^1 f(z') e^{-\chi z'} \, dz'.$$

We can define $\mathcal{I}^-$ and $\mathcal{I}^+$ in a similar way by replacing $f$ by $f_-$ and $f_+$ in the expression of $\mathcal{I}$. We can show $\mathcal{I}^-$ and $\mathcal{I}^+$ to be bounds for and $\mathcal{I}$ as follows:

$$\mathcal{I}(\chi) - \mathcal{I}^-(\chi) = \int_0^{1-\alpha} (f - f_-) e^{-\chi z'} \, dz'$$
$$+ \int_{1-\alpha}^1 (f - f_-) e^{-\chi z'} \, dz'. \quad \text{(B4)}$$

Since $f - f_-$ is positive between 0 and $1 - \alpha$ and negative between $1 - \alpha$ and 1, and $e^{-\chi z'}$ is a decreasing function of $z'$ ($\chi > 0$), lower bounds can be established for both terms on the right-hand side of Eq. (B4):

$$\int_0^{1-\alpha} (f - f_-) e^{-\chi z'} \, dz' \ge e^{-\chi(1-\alpha)} \int_0^{1-\alpha} (f - f_-) \, dz',$$

$$\int_{1-\alpha}^1 (f - f_-) e^{-\chi z'} \, dz' \ge e^{-\chi(1-\alpha)} \int_{1-\alpha}^1 (f - f_-) \, dz'.$$

Considering that $f - f_-$ averaged between 0 and 1 is zero, these two inequalities yield $\mathcal{I}(\chi) - \mathcal{I}^-(\chi) \geq 0$.

Similarly,

$$\mathcal{I}(\chi) - \mathcal{I}^+(\chi) = \int_0^\zeta (f - f_+)e^{-\chi z'}\, dz' + \int_\zeta^1 (f - f_+)e^{-\chi z'}\, dz'. \quad (B5)$$

Since $f - f_+$ is negative between 0 and $\zeta$ and positive between $\zeta$ and 1, and $e^{-\chi z'}$ is a decreasing function of $z'$, upper bounds can be established for both terms on the right-hand side of Eq. (B5):

$$\int_0^\zeta (f - f_+)e^{-\chi z'}\, dz' \leq e^{-\chi\zeta}\int_0^\zeta (f - f_+)\, dz',$$

$$\int_\zeta^1 (f - f_+)e^{-\chi z'}\, dz' \leq e^{-\chi\zeta}\int_\zeta^1 (f - f_+)\, dz'.$$

Considering that $f - f_+$ averaged between 0 and 1 is zero, these two inequalities yield $\mathcal{I}(\chi) - \mathcal{I}^+(\chi) \leq 0$.

Given the simple form of $f_-$ and $f_+$, $\mathcal{I}^-(\chi)$ and $\mathcal{I}^+(\chi)$ can be computed easily:

$$\mathcal{I}^-(\chi) = \frac{e^{-\chi}}{\chi}(e^{\alpha\chi} - 1) \quad \text{and} \quad \mathcal{I}^+(\chi) = \frac{\alpha}{\chi}(1 - e^{-\chi}).$$

Also, we can conclude that $\gamma$ has to be in the following range:

$$1 - \alpha\frac{e^\chi - 1}{e^{h/z_w} - 1} \leq \gamma \leq 1 - \frac{e^{\alpha\chi} - 1}{e^{h/z_w} - 1}. \quad (B6)$$

Since $\gamma$ is a set parameter, this gives us a range for $\chi$ and therefore for $\eta$:

$$h - \frac{z_w}{\alpha}\ln[\gamma + (1 - \gamma)e^{h/z_w}]$$
$$\leq \eta \leq$$
$$h - z_w \ln\left[1 + \frac{1 - \gamma}{\alpha}e^{h/z_w} - 1)\right]. \quad (B7)$$

This inequality provides the expressions for the bounds $\eta^-$ and $\eta^+$ on $\eta$ reported in Eq. (14).

Note that $\eta_-$ and $\eta_+$ both asymptotically approach the same linear function of $h$ for small $h$:

$$\eta^\pm \underset{h\to 0}{\sim} h\left(1 - \frac{1 - \gamma}{\alpha}\right). \quad (B8)$$

This is consistent with the existence of only one characteristic vertical scale for shallow, well-mixed ABLs.

## REFERENCES

Ackerman, A. S., and Coauthors, 2009: Large-eddy simulations of a drizzling, stratocumulus-topped marine boundary layer. *Mon. Wea. Rev.,* **137,** 1083–1110.

Bechtold, P., S. K. Krueger, W. S. Lewellen, E. van Meijgaard, C. H. Moeng, D. A. Randall, A. van Ulden, and S. Wang, 1996: Modeling a stratocumulus-topped PBL: Intercomparison among different one-dimensional codes and with large eddy simulation. *Bull. Amer. Meteor. Soc.,* **77,** 2033–2042.

Betts, A. K., and W. Ridgway, 1988: Coupling of the radiative, convective, and surface fluxes over the equatorial Pacific. *J. Atmos. Sci.,* **45,** 522–536.

——, and ——, 1989: Climatic equilibrium of the atmospheric convective boundary layer over a tropical ocean. *J. Atmos. Sci.,* **46,** 2621–2641.

Bony, S., and J.-L. Dufresne, 2005: Marine boundary layer clouds at the heart of tropical cloud feedback uncertainties in climate model. *Geophys. Res. Lett.,* **32,** L20806, doi:10.1029/2005GL023851.

Bretherton, C. S., and S. Park, 2008: A new bulk shallow cumulus model and implications for penetrative entrainment feedback on updraft buoyancy. *J. Atmos. Sci.,* **65,** 2174–2193.

——, J. Uchida, and P. N. Blossey, 2010: Slow manifolds and multiple equilibria in stratocumulus-capped boundary layers. *J. Adv. Model. Earth Syst.,* **2** (14), doi:10.3894/JAMES.2010.2.14.

Brown, A. R., and Coauthors, 2006: Large-eddy simulation of the diurnal cycle of shallow cumulus convection over land. *Quart. J. Roy. Meteor. Soc.,* **128,** 1075–1093.

Clement, A. C., R. Burgman, and J. R. Norris, 2009: Observational and model evidence for positive low-level cloud feedback. *Science,* **325,** 460–464.

Deardorff, J. W., 1972: Parameterization of the planetary boundary layer for use in general circulation models. *Mon. Wea. Rev.,* **100,** 93–106.

——, G. E. Willis, and D. K. Lilly, 1969: Laboratory investigation of non-steady penetrative convection. *J. Fluid Mech.,* **35,** 7–31.

Dufresne, J.-L., and S. Bony, 2008: An assessment of the primary sources of spread of global warming estimates from coupled atmosphere–ocean models. *J. Climate,* **21,** 5135–5144.

Holland, J. Z., and E. M. Rasmusson, 1973: Measurements of the atmospheric mass, energy, and momentum budgets over a 500-kilometer square of tropical ocean. *Mon. Wea. Rev.,* **101,** 44–55.

Klein, S. A., and D. L. Hartmann, 1993: The seasonal cycle of low stratiform clouds. *J. Climate,* **6,** 1587–1606.

Lenderink, G., and Coauthors, 2004: The diurnal cycle of shallow cumulus clouds over land: A single column model intercomparison study. *Quart. J. Roy. Meteor. Soc.,* **130,** 3339–3364.

Lilly, D. K., 1968: Models of cloud-topped mixed layers under a strong inversion. *Quart. J. Roy. Meteor. Soc.,* **94,** 292–309.

Matheou, G., D. Chung, L. Nuijens, B. Stevens, and J. Teixeira, 2011: On the fidelity of large-eddy simulation of shallow precipitating cumulus convection. *Mon. Wea. Rev.,* **139,** 2918–2939.

Moeng, C.-H., and Coauthors, 1996: Simulation of a stratocumulus-topped planetary boundary layer: Intercomparison among different numerical codes. *Bull. Amer. Meteor. Soc.,* **77,** 261–278.

Neggers, R. A. J., A. P. Siebesma, and T. Heus, 2012: Continuous single-column model evaluation at a permanent observational supersite. *Bull. Amer. Meteor. Soc.,* in press.

Norris, J. R., and C. B. Leovy, 1994: Interannual variability in stratiform cloudiness and sea surface temperature. *J. Climate,* **7,** 1915–1925.

——, and S. A. Klein, 2000: Low cloud type over the ocean from surface observations. Part III: Relationship to vertical motion and the regional surface synoptic environment. *J. Climate,* **13,** 245–256.

Nuijens, L., and B. Stevens, 2012: The influence of wind speed on shallow marine cumulus convection. *J. Atmos. Sci.,* **69,** 168–184.

Savic-Jovcic, V., and B. Stevens, 2008: The structure and mesoscale organization of precipitating stratocumulus. *J. Atmos. Sci.,* **65,** 1587–1605.

Schubert, W. H., J. S. Wakefield, E. J. Steiner, and S. K. Cox, 1979: Marine stratocumulus convection. Part II: Horizontally inhomogeneous solutions. *J. Atmos. Sci.,* **36,** 1308–1324.

Siebesma, A. P., and J. W. M. Cuijpers, 1995: Evaluation of parametric assumptions for shallow cumulus convection. *J. Atmos. Sci.,* **52,** 650–666.

——, and Coauthors, 2003: A large eddy simulation intercomparison study of shallow cumulus convection. *J. Atmos. Sci.,* **60,** 1201–1219.

Stevens, B., 2007: On the growth of layers of nonprecipitating cumulus convection. *J. Atmos. Sci.,* **64,** 2916–2931.

——, and Coauthors, 2001: Simulations of trade-wind cumuli under a strong inversion. *J. Atmos. Sci.,* **58,** 1870–1891.

——, and Coauthors, 2005: Evaluation of large-eddy simulations via observations of nocturnal marine stratocumulus. *Mon. Wea. Rev.,* **133,** 1443–1462.

——, A. Beljaars, S. Bordoni, C. Holloway, M. Köhler, S. Krueger, V. Savic-Jovcic, and Y. Zhang, 2007: On the structure of the lower troposphere in the summertime stratocumulus regime of the northeast Pacific. *Mon. Wea. Rev.,* **135,** 985–1005.

Uchida, J., C. S. Bretherton, and P. N. Blossey, 2010: The sensitivity of stratocumulus-capped mixed layers to cloud droplet concentration: Do LES and mixed-layer models agree? *Atmos. Chem. Phys.,* **10,** 4097–4109.

Wood, R., and C. S. Bretherton, 2006: On the relationship between stratiform low cloud cover and lower-tropospheric stability. *J. Climate,* **19,** 6425–6432.

Wyant, M. C., and Coauthors, 2007: A single-column model intercomparison of a heavily drizzling stratocumulus-topped boundary layer. *J. Geophys. Res.,* **112,** D24204, doi:10.1029/2007JD008536.

Xue, H., G. Feingold, and B. Stevens, 2008: Aerosol effects on clouds, precipitation, and the organization of shallow cumulus convection. *J. Atmos. Sci.,* **65,** 392–406.

Zhu, P., and Coauthors, 2005: Intercomparison and interpretation of single-column model simulations of a nocturnal stratocumulus-topped marine boundary layer. *Mon. Wea. Rev.,* **133,** 2741–2758.